

## 3D Reconstruction of a Rotating Erupting Prominence

W. T. Thompson<sup>1</sup> · B. Kliem<sup>2,3,4</sup> · T. Török<sup>5,6</sup>

© Springer ••••

**Abstract** A bright prominence associated with a coronal mass ejection (CME) was seen erupting from the Sun on 9 April 2008. This prominence was tracked by both the *Solar Terrestrial Relations Observatory* (STEREO) EUVI and COR1 telescopes, and was seen to rotate about the line of sight as it erupted; therefore, the event has been nicknamed the “Cartwheel CME.” The threads of the prominence in the core of the CME quite clearly indicate the structure of a weakly to moderately twisted flux rope throughout the field of view, up to heliocentric heights of 4 solar radii. Although the STEREO separation was 48°, it was possible to match some sharp features in the later part of the eruption as seen in the 304 Å line in EUVI and in the H $\alpha$ -sensitive bandpass of COR1 by both STEREO *Ahead* and *Behind*. These features could then be traced out in three-dimensional space, and reprojected into a view in which the eruption is directed towards the observer. The reconstructed view shows that the alignment of the prominence to the vertical axis rotates as it rises up to a leading-edge height of ≈2.5 solar radii, and then remains approximately constant. The alignment at 2.5 solar radii differs by about 115° from the original filament orientation inferred from H $\alpha$  and EUV data, and the height profile of the rotation, obtained here for the first time, shows that two thirds of the total rotation is reached within ≈0.5 solar radii above the photosphere. These features are well reproduced by numerical simulations of an unstable moderately twisted flux rope embedded in external flux with a relatively strong shear field component.

<sup>1</sup> Adnet Systems Inc., NASA Goddard Space Flight Center, Code 671, Greenbelt, MD 20771, USA

email: William.T.Thompson@nasa.gov

<sup>2</sup> Institut für Physik und Astronomie, Universität Potsdam, Potsdam 14476, Germany

<sup>3</sup> Mullard Space Science Laboratory, University College London, Holmbury St. Mary, Dorking, Surrey RH5 6NT, UK

<sup>4</sup> Part of this work was done while the author visited the Space Science Division of the Naval Research Laboratory, Washington, DC 20375, USA

<sup>5</sup> LESIA, Observatoire de Paris, CNRS, UPMC, Université Paris Diderot, 5 place Jules Janssen, 92190 Meudon, France

<sup>6</sup> now at Predictive Science, Inc., 9990 Mesa Rim Road, Ste. 170, San Diego, CA 92121, USA

---

**Keywords:** Corona, Active; Prominences, Active; Coronal Mass Ejections, Initiation and Propagation; Magnetic fields, Corona

## 1. Introduction

The bandpass of the inner coronagraph (COR1) telescopes on the two *Solar Terrestrial Relations Observatory* (STEREO) spacecraft runs from 650–670 nm (Howard *et al.*, 2008). This range was selected to include the hydrogen H $\alpha$  line at 656 nm, so as to be sensitive to erupting prominences associated with coronal mass ejections (CMEs). A particularly bright prominence eruption was observed by both COR1 telescopes on 9 April 2008. Although the relative contributions of H $\alpha$  emissions and Thomson-scattered light cannot be derived from the COR1 observations alone, it is presumed that H $\alpha$  is a significant contributor for the extremely bright parts of the prominence early in the eruption. This CME and prominence eruption was also observed by the STEREO *Extreme Ultraviolet Imager* (EUVI) telescopes (Howard *et al.*, 2008) before entering the COR1 field of view, as well as by TRACE at 171 Å (Handy *et al.*, 1999), and by the *Hinode* XRT telescope (Golub *et al.*, 2007) and EIS spectrometer (Culhane *et al.*, 2007). Landi *et al.* (2010) analyze this event, combining *Hinode*/XRT and EIS data, together with *Solar and Heliospheric Observatory* (SOHO)/UVCS/EIT/LASCO and STEREO/EUVI/COR1/COR2 images, to characterize the thermal properties of the ejected plasma, and constrain the heating rate. The post-CME current sheet following this event is analyzed by Savage *et al.* (2010) and Ko *et al.* (2010). Patsourakos and Vourlidas (2011) determine the geometrical parameters of the CME and post-CME current sheet in the field of view of the outer coronagraph (COR2) on STEREO. This event has become known as the “Cartwheel CME” because of the highly visible rotation around the line of sight seen during the initial stages of the eruption. Rotation about the vertical direction can also be observed through triangulation as the prominence material rises through the EUVI and COR1 height ranges. The plane of sky motions which give this event its “Cartwheel” name is actually a combination of the rotation about the vertical axis together with a deflection of the prominence in latitude and longitude during the initial rise phase. A rotation around the axis of the prominence, known as “roll effect” (Martin, 2003), may have contributed as well. Further rotation about the vertical direction is indicated by the CME orientation in the COR2 data. This paper presents an exploration of the rotation about the vertical direction in the EUVI and COR1 height ranges, using triangulation from the two STEREO viewpoints. The height profile of the rotation angle for the erupting prominence is obtained, which could not be done prior to the STEREO mission.

The separation of the two STEREO spacecraft at this time was 48°. Co-identification of features in both views is quite difficult with such a large separation. However, it was possible to match some sharp features in the later part of the eruption as seen by EUVI in the He II line at 304 Å. Features were also tracked in white light (with a possible H $\alpha$  component) as seen by COR1, although not necessarily the same features seen at 304 Å.



**Figure 1.** H $\alpha$  image of the filament as seen on the disk on 5 April 2008, 01:51 UT, before the first eruption on that day, and on 6 April, 02:44 UT (circled), reformed after the two eruptions on 5 April (from the Yunnan Astronomical Observatory in Kunming, China).

The derived height profile of prominence rotation is compared with the orientation of the polarity inversion line of the radial field component (PIL) at various heights, to check whether the rotation is simply the result of alignment with the PIL. The radial field component is obtained from a potential-field source-surface (PFSS) extrapolation. Additionally, the rotation and rise profiles of the prominence, as well as the STEREO images, are compared with the corresponding data obtained in a series of CME simulations in a companion paper (Kliem, Török, and Thompson, 2011; in the following Paper II), in order to explore a broader range of possible origins of the large total rotation observed. The comparisons suggest that the major part of the rotation was due to the presence of a shear field component of considerable strength in the source region (Isenberg and Forbes, 2007) and that the weak helical kink instability of a moderately twisted flux rope (Török, Kliem, and Titov, 2004) contributed as well. Field line plots of the best matching case are included here to demonstrate the correspondence with the observed overall shape and helical threads of the rising prominence.

## 2. Data Analysis

### 2.1. Source Region

The eruption on 9 April 2008 occurred in the remnants of NOAA active region (AR) 10989, located about 23° behind the west limb as seen from Earth, and

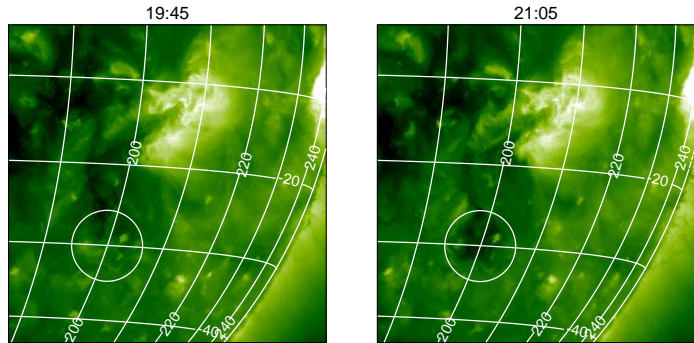


**Figure 2.** STEREO *Ahead* EUVI 195 Å images of AR 10989 before and after the second filament eruption on 5 April 2008, displaying an area of  $640''$  on a side. The image on the left at 19:45:30 UT shows the full extent of the filament on the southeastern end at the onset of the eruption (up to the middle of the circle), and the image on the right at 21:05:30 UT (with the circle plotted at the same position) shows that a dimming has developed at this location. Therefore, the erupting flux should be rooted in this area. Comparison with Figure 1 shows that only the upper branch of the filament is visible in H $\alpha$ . Overplotted grid lines represent Carrington longitude and latitude.

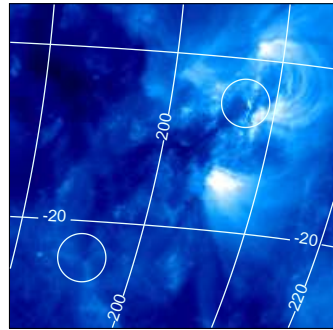


**Figure 3.** STEREO *Ahead* EUVI 171 Å image of the reformed filament on 6 April 2008, 15:01 UT. The area shown is  $320''$  on a side. The circles mark the ends of the filament material visible at this wavelength. Their distance is  $\approx 175$  Mm. The main body of the filament as seen in this line is oriented at an inclination of  $\approx 26^\circ$  to the east-west direction on the Sun.

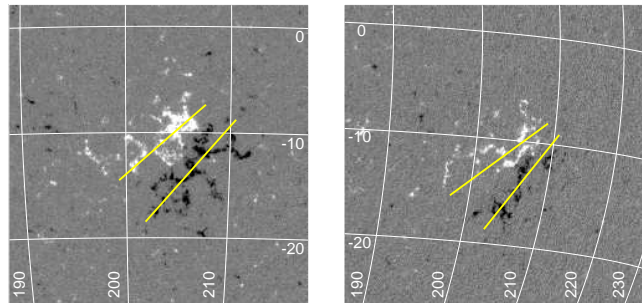


**Figure 4.** Magnetogram of AR 10989 on 31 March (*left*) and on 4 April 2008 (*right*) taken by SOHO/MDI. The overplotted bars indicate rough estimates of the distance between the center of each polarity (in a center-of-gravity sense), which is an important input parameter for the numerical modeling of the event in Paper II.

---

had an onset time near 09 UT. The filament had been visible nearly throughout the disk passage of the active region, which was in its decaying stage and spotless after 31 March. The filament erupted twice on 5 April 2008, reforming afterwards. These eruptions were visible on disk to EUVI on STEREO *Ahead*. Both eruptions appeared to propagate inclined from the radial direction toward higher southern latitudes, similar to the eruption on 9 April. The inclination made it difficult to discern rotational motions based on images from only a single viewpoint. However, a stereoscopic reconstruction of the second eruption revealed a considerable rotation of about 90° (Bi *et al.*, 2011). Interestingly, the rotation was in the clockwise direction, opposite to that of the eruption on 9 April.

As with most filaments, it is difficult to discern the magnetic connections at its ends. However, both eruptions on 5 April produced a dimming and endpoint brightenings in the EUV (Wang, Muglach, and Kliem, 2009) near the southeastern end of the filament, which were located in negative polarity, the polarity which dominated the southwestern side of the filament channel, so that the filament was dextral according to the classification of Martin (1998). This is further supported by the right-bearing orientation of the filament barbs (see Figure 1). Dextral filaments are embedded in field of left handed chirality, as indicated by the typical skew of the overlying arcade of coronal loops (Martin, 1998). If the assumption of flux rope topology holds for the filament, then the filament itself is also threaded by left-handed field. Otherwise, it may have the opposite chirality (see Martin and McAllister, 1997; Ruzmaikin, Martin, and Hu, 2003; Muglach, Wang, and Kliem, 2009). If a filament in dominantly left-handed helical field rotates upon eruption, the direction of rotation is generally found to be in the counter-clockwise direction, as expected from helicity conservation (Rust and LaBonte, 2005; Green *et al.*, 2007).

Note that the dextral chirality of the filament is an exception to the usual hemispheric rule (Martin, Bilimoria, and Tracadas, 1994). However, Pevtsov, Balasubramaniam, and Rogers (2003) show that 16–25% of filaments do not follow the hemispheric rule, and that the rule is weaker for filaments in active regions.

On 5 April, the filament was oriented at an inclination of  $\approx 24^\circ$  to the east-west direction on the Sun and had a length of  $\approx 135$  Mm in the image shown in Figure 1 (top). However, the dimmings and endpoint brightenings formed in the eruptions later on the same day suggest that the true extent of the flux in the filament channel was larger by about one third,  $\approx 175$  Mm, see Figure 2.

Due to foreshortening, the H $\alpha$  images on the following day show the filament, its magnetic connections and barbs far less clearly, but it can be seen that the filament reformed in a similar location (Figure 1, bottom). The better perspective of the EUVI-*Ahead* images indicates that the main body of the reformed filament was nearly straight, oriented at a tilt angle of  $\approx 26^\circ$  to the east-west direction, and extended across a similar length as on 5 April (Figure 3). This is most clear if the 171 Å and 304 Å images are viewed in animated format. As far as the increasing foreshortening allows a judgment, the filament appeared to keep its orientation and shape through the subsequent days until a new eruption launched the Cartwheel CME.

Since the numerical modeling in Paper II reveals a strong influence of the distance between the polarities in the source region on the rotation of the ejected

---

flux rope, we attempt to estimate this parameter. Figure 4 shows magnetograms of the region from the SOHO Michelson Doppler Imager (MDI) on 31 March and 4 April 2008. The overplotted bars run through the middle of each polarity in a one-dimensional center-of-gravity sense, providing an indication of the distance between the main polarities. This value increases from  $\sim 40$  Mm to a range of  $\sim(40\text{--}75)$  Mm over the four-day time span. A range twice as wide may have been characteristic of the configuration after the similar time span to the eruption on 9 April. It appears impossible to estimate a single relevant value. We will adopt a distance of 90 Mm as a base value in most simulations in Paper II, but also study the influence of its variation. This base value lies in the middle of the estimated range, so it is consistent with the fact that much of the rotation occurred in the course of the radial ascent above the south-east edge of the remnant active region, which is characterized by a considerable distance between the polarities (see Section 2.3).

The magnetograms in Figure 4 show an overall displacement of the two polarities in the direction of the PIL. While the negative flux is more or less uniformly distributed along the filament channel, the positive flux is more concentrated near the northern end. This results in a net shear field component pointing along the filament channel in the southeastward direction. Coronal field lines that arch above the filament thus possess a skew corresponding to the upper part of a left-handed helix, in agreement with the implication made above that the filament was dextral.

We have also estimated the height of the prominence from data taken by the EUV Imaging Telescope (EIT) (Delaboudinière *et al.*, 1995) onboard SOHO on 8 April, when the prominence was close to the limb. The material seen at that time in the 304 Å line extended up to a height of  $\approx 0.04 R_\odot$  above the photosphere, and the absorbing material seen at 171 and 195 Å extended up to  $\approx 0.033 R_\odot$ . From EUVI 304 Å data about an hour before the eruption, we estimate the height to lie in the range  $\approx 0.05\text{--}0.06 R_\odot$ , so it is clear that the prominence experienced a slow rise before the eruption.

Motions along the prominence could be seen in the 171 Å channel of EUVI-*Ahead* on 9 April from about 08:20 UT onward. The first upward motions of prominence material along the CME path can be discerned by comparing the images at 08:48:30 and 08:51 UT. Landi *et al.* (2010) give a rather conservative estimate of the CME start time, 09:10 UT, but the 171 Å images, taken at 2.5 min cadence, show that most of the prominence body visible to EUVI-*Ahead* was already moving by 08:53:30 UT, the start time quoted in Savage *et al.* (2010). Since the event commenced in the absence of a strong perturbation (no signs of a significant brightening, of a jet, or of perturbations resulting from nearby activity were seen), it must have developed from a small perturbation when the configuration was near the boundary between stable and unstable states. In such cases the initial motion of the unstable flux is expected to behave exponentially, which requires some time to develop to a level that causes visible changes. Rapid changes in the vertical position were first seen between the EUVI-*Ahead* images at 08:48:30 and 08:51 UT. Therefore, the actual start time should lie before 08:51 UT.

A helmet streamer, best seen in the COR2-*Ahead* images, extended above AR 10989 in the plane-of-sky projection. In order to estimate the orientation of

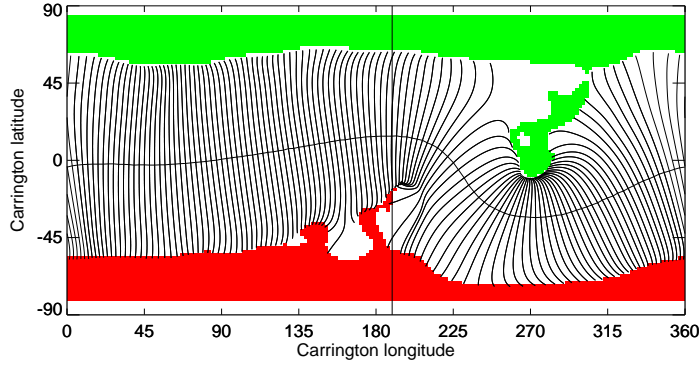


**Figure 5.** Location of the heliospheric current sheet for Carrington Rotation 2068 from a potential-field source-surface extrapolation. The current sheet runs nearly east-west above the estimated CME direction of propagation as indicated by the vertical bar. The green and red regions represent open field regions of negative and positive polarity respectively.

the heliospheric current sheet above the streamer, and whether it was magnetically connected with the PIL in the active region, we ran a PFSS extrapolation and a Wang-Sheeley-Arge model for Carrington Rotation 2068 at the Community Coordinated Modeling Center (CCMC), using a source surface location at 2.5 solar radii for both models. Figure 5 shows the PIL and corresponding field lines originating at the  $2.5 R_{\odot}$  source surface of the PFSS model, which yields a nearly east-west orientation of the heliospheric current sheet at the longitude of radial CME propagation estimated in Section 2.3. The Wang-Sheeley-Arge model gives the same result. It is clearly seen that the field at large heights above the active region is dominated by the large-scale field of the Sun, which points essentially opposite to the shear field component in the active region at small heights.

A similar representation of the radial field component of the PFSS model at several representative heights is given in Figure 6. The PIL above AR 10989 is part of a magnetic structure which is distinct from the PIL at the base of the heliospheric current sheet, and which is seen as a separate ring in the low corona (*e.g.* at  $1.15 R_{\odot}$ ). With increasing height, the ring-shaped PIL disappears (between 1.2 and 1.3 solar radii), and the PIL associated with the heliospheric current sheet gradually approaches the equator at the estimated longitude of the CME.

## 2.2. 3D Reconstruction

The SolarSoft routine `scc_measure` was used to measure the three-dimensional location of features in the STEREO EUVI and COR1 images. The action of

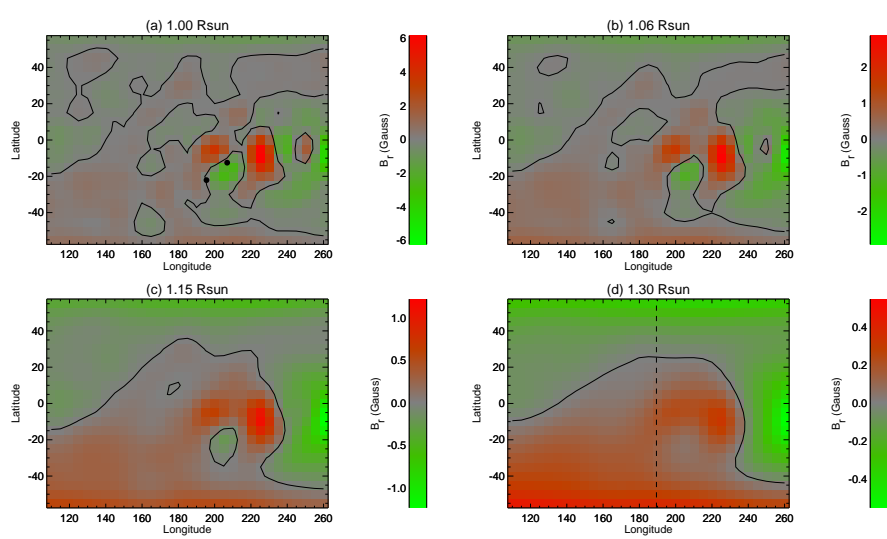


**Figure 6.** Polarity inversion line of the radial field component in the PFSS model, (a) in the photosphere, (b) at the estimated initial height of the prominence, (c) at the largest height that shows an orientation of the PIL above AR 10989 relatively clearly, and (d) at  $1.3 R_{\odot}$  where the PIL above AR 10989 is completely gone. Dots in panel (a) mark the end points of the prominence shown in Figure 3, and the vertical line in panel (d) marks the estimated longitude of the CME, as in Figure 5.

this program is as follows: The user is presented with two side-by-side images, one from each of the two STEREO spacecraft. The images are selected so that they represent the same observation time, with a slight offset to account for the difference in light travel time from the Sun. The user can zoom in on the region of interest in the two images, and adjust the color table and data range to optimize the appearance of the feature being measured. A point is selected on one image with the cursor. The program calculates the three-dimensional line of sight represented by this point, and then overplots the projection of this line onto the image from the other satellite. This is known as an epipolar line. Since both the EUVI and COR1 optics produce a gnomonic projection on the CCD detector, straight lines in space will always appear as straight lines in the image. The feature selected by the user in the first image must appear along the epipolar line drawn by the program in the second image. The correct location along this line is selected by the user, which leads to another line of sight calculation which intersects the original line of sight. The intersection of these two lines determines the three-dimensional (3D) location of the feature. In this investigation, we use this technique to find the 3D locations of multiple points along prominence threads.

The main difficulty in applying this technique to the prominence eruption is source confusion. On 9 April 2008, the two STEREO spacecraft were separated by  $48^{\circ}$  along the ecliptic plane. Thus, the appearance seen by STEREO *Ahead* was quite different from that seen by STEREO *Behind*. This made it very difficult to locate features which could be positively identified to be the same in both images. Another goal was to identify features which could be tracked through

---

several frames. (However, no attempt was made to match identifications between EUVI and COR1.) In spite of these difficulties, it was possible to identify several features which could be identified in both views, and which could be tracked through several frames.

### 2.3. EUVI and COR Measurements

Figures 7 and 8 show the tracked features as seen in the 304 Å channel of EUVI-*Ahead*. The colored lines represent the filamentary features that were measured at each time step. Each line has a different color, and a dot at one end, to better show the relationship with the reprojected graphs along the right side. The different colors do not necessarily represent the same threads at each time step. The He II 304 Å channel was chosen as being most representative of the cool prominence material seen later in a combination of H $\alpha$  and Thomson-scattered light by COR1. Although the eruption is clearly seen by *Ahead* at 9:06 UT, and by *Behind* at 9:36 UT, source confusion made it impossible to track features earlier than 10:06 UT. Initially, little sense could be made from an examination of these data viewed in 3D (*e.g.*, through an anaglyph representation). However, because the measurements are made in 3D, they can be reprojected to another viewpoint. By selecting the proper viewpoint, it's possible to see aspects of the data that are not evident in the frame in which the data are taken. The plots to the right in Figures 7 and 8 show the same data as in the images, but from a viewpoint at Stonyhurst longitude 98° west (relative to Earth), and 24° south. It is estimated that from this viewpoint, the CME is traveling straight toward the observer.

From this perspective, a certain organization can be perceived. The primary alignment in the 10:06 UT data is vertical, *i.e.* aligned north-south, with the upper prominence threads lying almost directly over the lower threads in the frame of the figure. However, in the later images the primary alignment is distinctly sloped, with the upper threads lying toward the east, and the lower ones toward the west. This is particularly well seen in the image at 10:46 UT in Figure 8, where the data display an overall slope of  $-50^\circ$ . As one goes through the time steps, a counter-clockwise rotation can be perceived as one steps from 10:06 to 10:46 UT.

The prominence structure must have rotated through  $\approx 65^\circ$  from its original orientation to achieve the nearly north-south structure seen at 10:06 UT, followed by an additional  $\approx 50^\circ$  to reach the maximum rotation at 10:46 UT. Thus, the full amount of rotation experienced by the prominence in the EUVI height range was on the order of  $115^\circ$ .

The EUV observations of the early part of the eruption also show a shift of the entire prominence structure southward, from about  $-14^\circ$  to  $-24^\circ$  latitude. Compared with the earlier H $\alpha$  observations (Figure 1), the prominence must have also shifted  $\sim 15^\circ$  eastward in the early phase of the eruption. These initial motions were followed by radial propagation at the new latitude and longitude,  $\approx 98W24S$ . This is consistent with the analysis of Savage *et al.* (2010) and Patsourakos and Vourlidas (2011). The latter authors fitted a croissant-shaped flux rope model to COR2 images from both STEREO satellites and

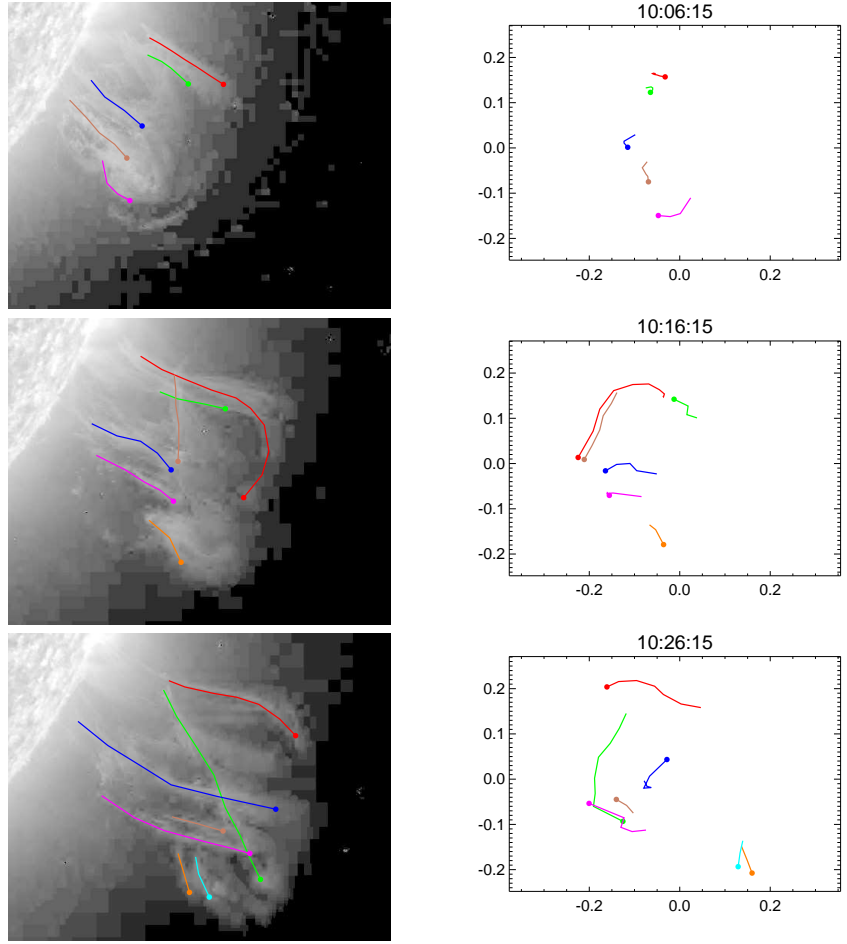


**Figure 7.** Images and plots of the prominence eruption from 10:06 to 10:26 UT, as seen in the 304 Å channel of the STEREO EUVI telescopes. Subsequent frames are shown in Figure 8. Along the left are shown the EUVI-*Ahead* images with the tracked features overplotted. The lower-right corner of each image is outside the EUVI field of view, causing the threads to appear truncated in height at 10:26 UT and subsequent times. The plots along the right show the same data reprojected to a viewpoint at Stonyhurst longitude 98° west (relative to Earth) and latitude 24° south. Axes are in units of solar radii.

found that the radial propagation of the CME projects back to a position  $11^\circ \pm 5^\circ$  behind the limb, as seen from Earth, and  $17^\circ \pm 3^\circ$  south. Savage *et al.* (2010) quote a heliographic position of  $113^\circ$  for the associated active region at the time of the eruption, and describe the initial motion of the prominence as being toward the observer. The measurements shown in Figures 7 and 8 were derived from the radial phase of the eruption.

The same analysis performed on EUVI was also performed on the COR1 images. At the location of the eruption, the COR1-*Ahead* occulter edge is at 1.37 solar radii, and the COR1-*Behind* edge is at 1.59 solar radii. The features

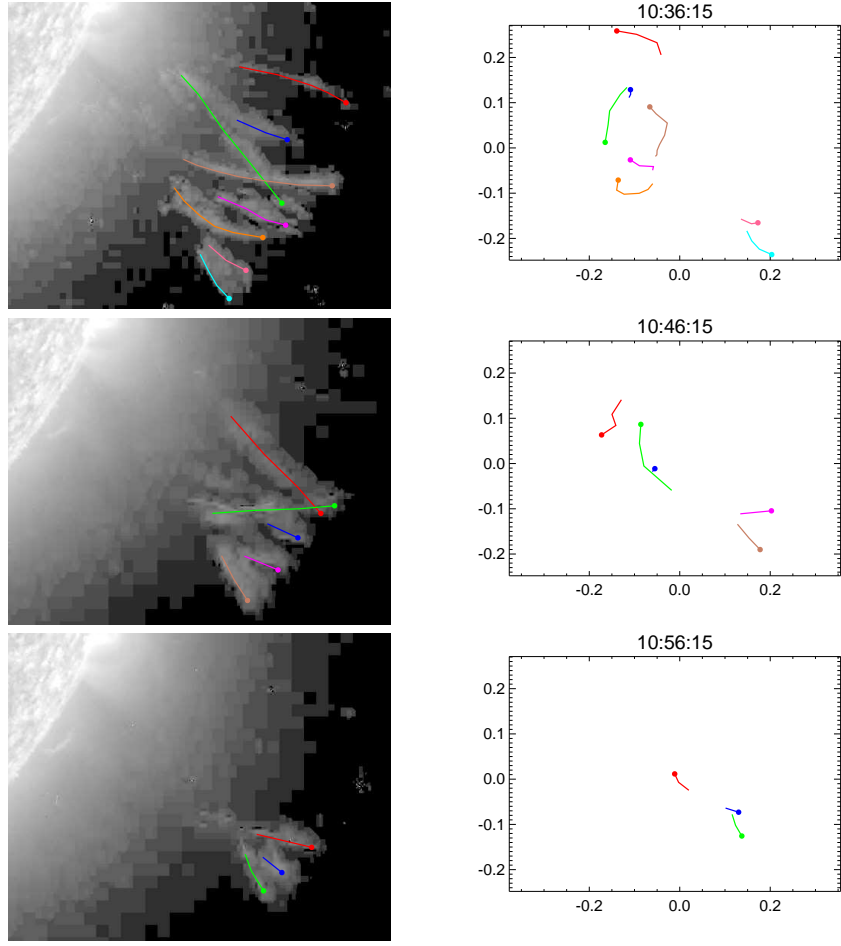


**Figure 8.** Continuation of Figure 7 for time steps 10:36 to 10:56 UT.

seen by COR1 are a continuation to higher radial distances of the truncated 304 Å features seen by EUVI. There is a small region of overlap between EUVI and COR1 on both spacecraft, and the observations agree within this region. The COR1 results are shown in Figure 9. The prominence is seen to maintain the orientation seen in the final EUVI images. There is a slight indication of a shift back in the clockwise direction. However, the orientations for the final two time steps at 11:15 and 11:25 UT are based on only parts of the prominence legs, so the apparent reverse rotation may not truly represent the behavior of the loop as a whole.

Patsourakos and Vourlidas (2011) estimated the orientation of the CME flux rope from their croissant model fit at a leading-edge heliocentric distance of about  $13 R_{\odot}$ . They found that the flux rope (croissant) axis was inclined to the east-west direction on the Sun by a tilt angle of  $-4^{\circ} \pm 7^{\circ}$ . This indicates a

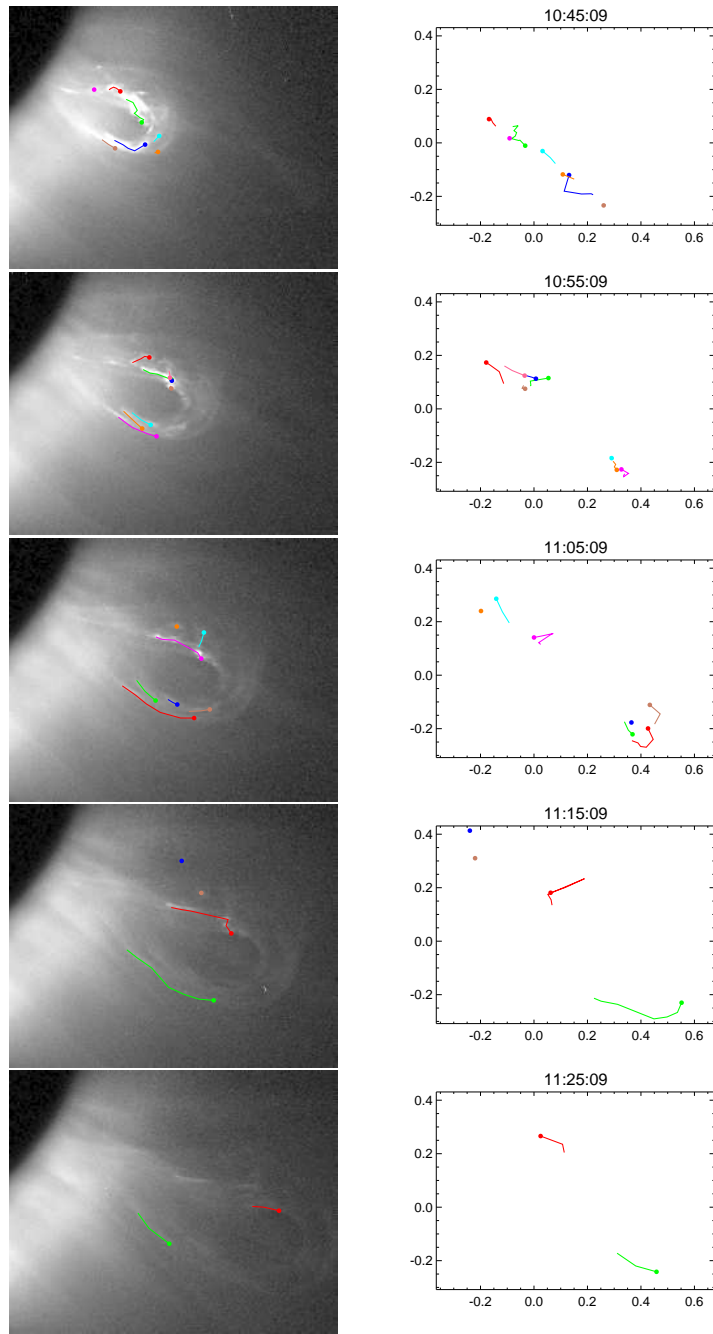


**Figure 9.** Images and plots of the prominence eruption from 10:45 to 11:25 UT, as seen in the COR1 telescopes. Along the left are shown the COR1-*Ahead* images with the tracked features overplotted. The plots along the right show the same data reprojected to a viewpoint at Stonyhurst longitude 98° west (relative to Earth) and latitude 24° south. Axes are in units of solar radii.

---

further counter-clockwise rotation to a total value of  $150^\circ \pm 7^\circ$  from the original orientation estimated in Section 2.1. (The other possible interpretation of a clockwise rotation by  $\approx -145^\circ$  following the counter-clockwise rotation in the EUVI height range appears far less likely.) It should be noted that the croissant model does not include any writhe of its axis, so that the uncertainties may be higher; however, this is not expected to change the result by a large amount. The rotation angle at large heights represents a close alignment of the CME flux rope with the heliospheric current sheet (Figure 5), which corresponds to the suggestion in Yurchyshyn (2008) and Yurchyshyn, Abramenko, and Tripathi (2009).

To our knowledge, the rotation of the prominence by  $\approx 115^\circ$  in the corona and by  $\approx 150^\circ$  up to  $13 R_\odot$  belongs to the largest ever inferred in this height range. Yurchyshyn, Abramenko, and Tripathi (2009) report one case of rotation by  $\approx 143^\circ$  and six cases in the range  $80^\circ$ – $100^\circ$  out of a sample of 101 halo CMEs observed by SOHO/LASCO, *i.e.*, up to a distance of  $30 R_\odot$ . The largest rotation found at 1 AU is on the order of  $160^\circ$  (Dasso *et al.*, 2007; Harra *et al.*, 2007).

It is also of interest to note that the COR1 images resolve the basic structure of the dense prominence material in the core of the CME out to a heliocentric distance of four solar radii. The CME core has the structure of a weakly to moderately twisted flux rope: a single flux loop with threads that are systematically but only weakly to moderately inclined to the axis of the loop. These indications of twist prove to be the primary observational finding that sets a preference for a slightly kink-unstable flux rope above a kink-stable flux rope, which match the observed rise and rotation characteristics to a comparable degree in the numerical modeling of the event in Paper II. Only few observations have revealed a flux rope structure for an erupting prominence so clearly in this height range (see, *e.g.*, Plunkett *et al.*, 2000). The images also indicate a nearly self-similar evolution of the flux rope throughout the instrument's field of view of (1.5–4)  $R_\odot$ . The outer coronagraph COR2 imaged the CME core as well but did not resolve the details of its structure.

#### 2.4. Rotation and Rise Profile

Figure 10 summarizes the rotation of the erupting prominence as a function of time from both EUVI and COR1. The values plotted were obtained by averaging the orientations of the individual threads whose 3D positions could be reconstructed. The values obtained at 10:16 and 10:26 UT are considered to be less reliable than the others in the figure, since at these times the threads which could be located in 3D do not appear to be organized in a well defined structure, as, for example, flux rope legs (see the right panels in Figure 7). It was not possible to derive the 3D prominence orientation for times before 10:06 UT due to source confusion. However, the visible appearance of the prominence as seen from STEREO *Ahead* between 9–10 UT is consistent with considerable rotation throughout this time period, leading to the conclusion that most of the rotation occurred during the initial phase of the eruption.

We also used `scc_measure` to derive a time-height curve for the prominence eruption. This was done by matching points at the leading edge of the prominence in both images. Since these points in the two images are not guaranteed

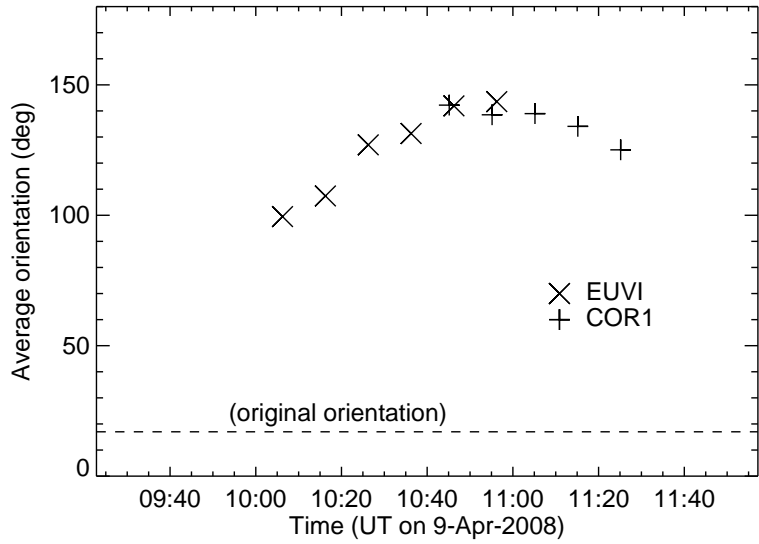


**Figure 10.** Orientation of the prominence body as a function of time. The dashed line represents the original orientation as estimated from the EUVI-*Ahead* 171 Å image on 6 April in Figure 3. The points at 10:16 and 10:26 UT are considered to be less reliable than the others—see text.

to represent exactly the same point in 3D space, the results can only be treated as an approximation. However, since the extent of the prominence material is relatively small, the approximation is quite valid. The resulting time-height curve for the top of the prominence is shown in Figure 11. The COR1 values appear to be a bit higher than one would expect from an extrapolation of the EUVI data. That may represent a difference between the appearance of the prominence at 304 Å versus white light. In addition, the heights derived from EUVI data after 9:56 UT may systematically fall short of the true heights. It is possible that the traceable threads did not extend up to the true top of the structure in these images, since an upward extension of the loop-shaped structure in the image at 9:56 UT had faded by 10:06 UT. The estimated height at 10:26 UT is only a lower limit given by the edge of the EUVI-*Ahead* field-of-view.

A quadratic fit to the EUVI data gives an initial speed of  $67 \text{ km s}^{-1}$ , accelerating to  $173 \text{ km s}^{-1}$  as the prominence leaves the EUVI field-of-view. A quadratic fit to the heights measured by COR1 gives a velocity starting at  $206 \text{ km s}^{-1}$ , and accelerating to  $379 \text{ km s}^{-1}$  by the end of the COR1 data. There's some evidence from the COR1 quadratic fit that the acceleration strongly decreased when the leading edge of the prominence reached a heliocentric height of 3 solar radii. This is borne out by a linear fit to the COR1 data points above 3 solar radii, which gives a slightly lower velocity of  $327 \pm 9.2 \text{ km s}^{-1}$ . The combined EUVI and COR1 data in Figure 11 give the visual impression that much of the acceleration actually occurred up to  $\approx 2.5$  solar radii. The COR2 data give a

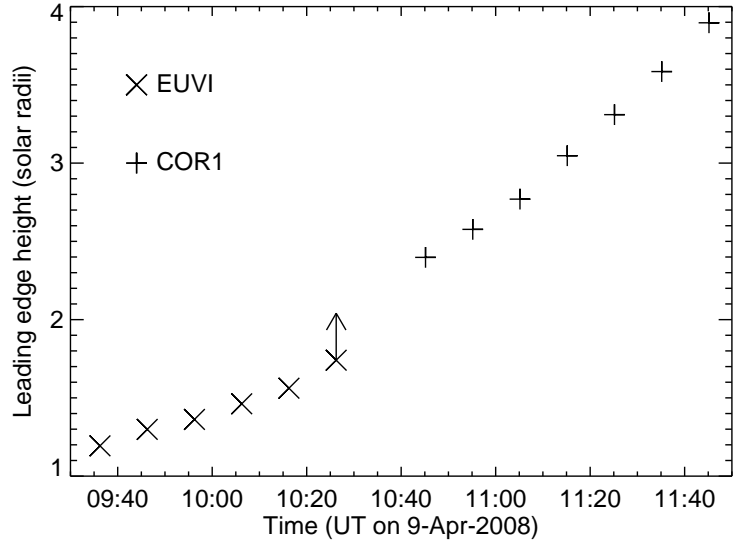


**Figure 11.** Heliocentric heights of the prominence leading edge *vs.* time. The value for 10:26 UT is shown as a lower limit, since the prominence is right at the edge of the EUVI-*Ahead* field-of-view at this time.

speed close to  $400 \text{ km s}^{-1}$ . All of these values refer to estimated positions of the apex point of the visible flux rope structure in the core of the CME.

Landi *et al.* (2010) also derive a time-height profile for the leading edge of the prominence material, using a combination of STEREO *Ahead* and SOHO data. Their results are very close to those presented here, with the possible exception of the amount of acceleration. Landi *et al.* quote an acceleration of  $59.6 \text{ m s}^{-2}$ , while our results are more consistent with a smaller value of  $37.9 \pm 4.0 \text{ m s}^{-2}$  over the time range covered by Figure 11. They also give the projected velocity of the CME leading edge in the plane of the sky of STEREO *Ahead*, which approaches  $700 \text{ km s}^{-1}$ , still rising, at a heliocentric height of  $3 R_{\odot}$ .

Combining the information in Figures 10 and 11, we obtain the rotation of the prominence as a function of its leading edge height, see Figure 12. (As there are only three time steps in common between the EUVI data sets, we have interpolated the EUVI and COR1 height data from Figure 11 to the times of the EUVI measurements in Figure 10 to better show the trend.) These data emphasize again that much of the rotation is acquired in the height range  $h \lesssim R_{\odot}/2$ , or  $\sim 2$  initial footpoint separations, above the photosphere.

## 2.5. Comparison With the Orientation of the PIL

The comparison of the PFSS extrapolation with the orientation of the prominence at large distances from the Sun obtained in Patsourakos and Vourlidas (2011) shows that the prominence has approached a close alignment with the

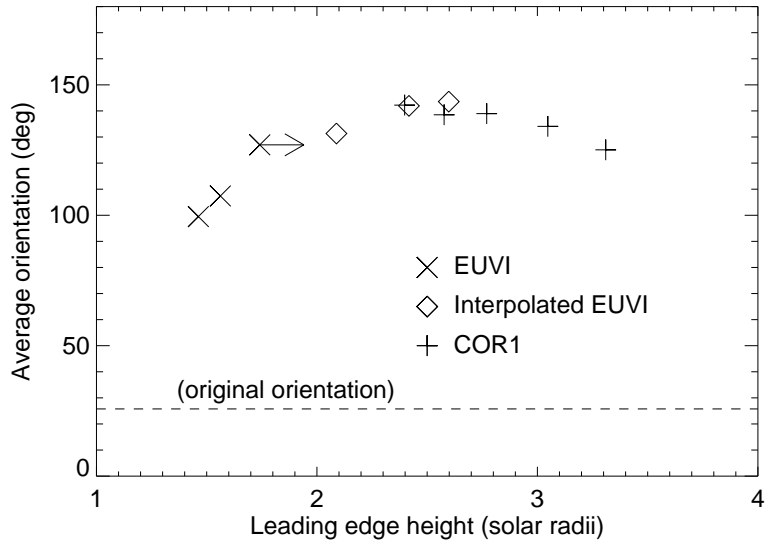


**Figure 12.** Prominence rotation *vs.* heliocentric height of its leading edge. The diamond symbols represent EUVI and COR1 height data from Figure 11 interpolated to the times of EUVI orientation measurements in Figure 10.

heliospheric current sheet (Section 2.3). An obvious question is whether such alignment could also lead to the rotation in the coronal height range studied here. We will see in Paper II that the rotation of erupting flux ropes and the change of the PIL orientation with height always point in opposite directions if the eruption originates in a simple bipolar region. However, Figure 6 shows that the topology of the field above AR 10989 is more complex. In particular, the field component along the filament channel, which influences the rotation of erupting flux (Isenberg and Forbes, 2007), changes sign with increasing height. In Figure 6, it is clearly seen that the relevant section of the PIL keeps a nearly constant orientation up to about  $1.15 R_{\odot}$ , above which it starts to shrink noticeably, disappearing completely by  $1.3 R_{\odot}$ . Thus, any rotation in the height range up to about  $1.15 R_{\odot}$  could not be caused by a changing PIL direction. In the height range  $\approx (1.15-1.3) R_{\odot}$  the prominence did not see a PIL with a well defined direction. Above  $1.3 R_{\odot}$ , the prominence entered the large-scale field structure defined by the polar fields and the heliospheric current sheet. The PIL direction in this range is relatively similar to the direction of the photospheric PIL in the active region and the original orientation of the prominence. Hence, throughout the height range of strong initial prominence rotation,  $\sim (1-1.5) R_{\odot}$ , the assumption of rotation by alignment with the relevant PIL is inconsistent with the structure of the field. The prominence actually rotated away from the PIL in this height range.

The situation changed when the initial prominence rotation began to level off at a large angle. The subsequent rotation up to the height considered in

---

Patsourakos and Vourlidas (2011) is consistent with an alignment with the PIL in the heliospheric current sheet. From the orientation reached in the initial phase, it was favorable for the prominence to continue the rotation to align with the PIL nearly antiparallel to the original orientation.

These conclusions are robust against the limitations of the PFSS model, which reflects the magnetic structure in and around AR 10989 primarily at the time of central meridian passage, since the region did not show any strong magnetic changes in the time before the eruption on 9 April. The orientation of the PIL in the photosphere, as outlined by the prominence in the EUV, changed by about 20°, much smaller than the observed prominence rotation in the low corona. No signs were seen of any major flux emergence which might have altered the topology of the ring-shaped PIL seen at low coronal heights.

Generally, one expects a dominance of the Lorentz force in driving any rotation of erupting flux at low coronal heights, where the plasma beta is small. As summarized in the following section and detailed in Paper II, the Lorentz force due to both the tension of twisted field lines and the presence of a shear field component in the ambient field causes a rotation away from the PIL, along which the rising flux is originally oriented. As larger heights are reached, the currents and Lorentz forces in the erupting flux decrease, while the influence of the pressure gradient force increases with the increasing plasma beta in the ambient field. The alignment with the heliospheric current sheet then reaches an increasing importance in the dynamics of the eruption. The transition is expected to occur when the plasma beta approaches unity.

A difference between the PIL in AR 10989 and the large-scale PIL in the streamer should be noted. While the PILs are nearly parallel to each other, the field direction across them is reversed (Figure 6). The horizontal field component across the PIL in the streamer exerted a Lorentz force on the prominence legs according to the mechanism proposed in Isenberg and Forbes (2007), because the prominence was directed approximately along this field component (perpendicular to the PIL) after the initial rotation had leveled off, *i.e.*, in the whole COR1 height range. With the current flowing opposite to the axial field of the dextral prominence, the direction of this force on the legs of the prominence is such that the top part rotates in the clockwise direction. This might explain the slight backward rotation indicated by the COR1 data. If this were the dominant effect in the subsequent evolution, the initial rotation would be reversed until the prominence aligns with the heliospheric current sheet in the direction parallel to its original orientation. Since the transition to high-beta conditions occurs in the COR1-COR2 height range, it is unlikely that the Lorentz force could dominate the subsequent rotation. Consequently, antiparallel alignment with the PIL in the heliospheric current sheet due to the pressure gradient force, which drives such alignment on the shortest possible path, independent of the field direction, appears to be the most likely evolution in the COR2 height range.

### 3. Numerical Modeling

Paper II presents a parametric study of various effects which lead to, or influence, the rotation of ejected flux ropes in low-beta plasma. The initial flux rope twist,

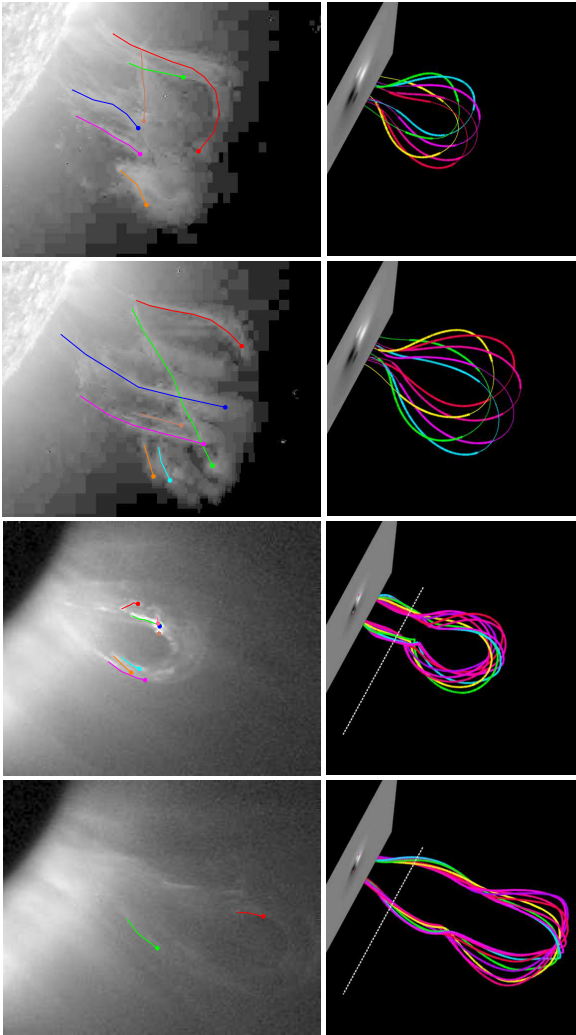


**Figure 13.** Shape of the erupting flux in the best-matching numerical model — a weakly kink-unstable flux rope of initial twist  $3.5\pi$  — at various stages of the rise, compared with STEREO Ahead images at 10:16, 10:26, 10:55, and 11:25 UT. A set of field lines enclosing the magnetic axis of the simulated flux rope is plotted at the times the rope apex has reached the corresponding heights,  $h = 7.3, 9.6, 20$ , and  $30 h_0$  ( $h_0$  — initial apex height), which are obtained from the scaling of the footpoint distance,  $3.3 h_0$ , to the value of 175 Mm estimated in Section 2.1. The observed and simulated flux ropes are displayed at the same perspective: the line connecting the footpoints of the rope makes an angle of  $26^\circ$  with the line of sight and the vertical axis in the simulation is tilted away from the observer by  $8^\circ$  (so that the magnetogram,  $B_z(x, y, 0, t)$ , is seen from the bottom side). The dotted line indicates the edge of the COR1 occulting disk. Since the visible threads in the EUVI images do not outline the complete shape of the flux rope, sections of the field lines in the corresponding simulation snapshots are highlighted for better visual correspondence. For each field line, 200 segments at the top and 150 segments at each bottom end are plotted with reduced line width. The segments are obtained from a numerical integration along the field line with adaptive step size and are all different, resulting in different lengths of the highlighted sections, analogous to the observations.

---

the strength of the external shear field component, and the height profile of the overlying potential field are varied. The latter is related to the distance between the main polarities in the photosphere. Figure 13 shows field line plots from the numerical model that best fits the observations in their entirety (rise and rotation profiles and the STEREO images). In this model, a moderate initial twist of  $\Phi = 3.5\pi$  triggers a weak helical kink instability, which lifts the initially force-free, toroidal flux rope into the torus-unstable range of heights and also contributes to the rotation. The ejection is primarily driven by the torus instability (Kliem and Török, 2006), so that the model belongs to the loss-of-equilibrium category (Priest and Forbes, 2002). The major part of the rotation in this run is due to the presence of an external shear field component (pointing along the prominence and polarity inversion line and due to sources outside the flux rope), as first suggested in Isenberg and Forbes (2007). The strength of the shear field at the initial flux rope apex is  $2/3$  of the external poloidal field which holds the rope in equilibrium. The value is consistent with a very rough estimate of this ratio from the structure of the active region. The ratio of the distances between the main polarities along and across the PIL is about  $1/2$  in the PFSS field, and the shear should slightly increase with the gradual change of the PIL direction in the time till the eruption.

The overall shapes of the flux rope in the considerable height range included in Figure 13, as well as the inclination of the still weakly twisted field lines to the axis of the rope at the largest height, match the observations reasonably well. (Note that the rope has acquired a large part of its total rotation already at the first time selected; see Figure 10.) Similar agreement is demonstrated in Paper II for the height-rotation and time-height profiles.

A model with subcritical initial twist,  $\Phi = 2.5\pi$ , which allows only for the development of the torus instability, reproduces the rise profile similarly well, while the match with the rotation profile is somewhat worse. The field lines at the strongly expanded stage of the final COR1 image in Figure 13 are rather straight and hardly show any indication of the observed twist. Moreover, this flux rope requires a considerable initial perturbation to reach the torus-unstable range of heights, which is not supported by the pre-eruption height estimate and the initial dynamics of the prominence described in Section 2 (see Paper II).

#### 4. Summary and Conclusions

The images of the STEREO EUVI and COR1 telescopes resolve the basic structure of the erupting prominence in the core of the “Cartwheel CME” on 9 April 2008 out to heliocentric distances of  $4 R_\odot$ . A single flux rope with indications of weak to moderate twist is revealed. The flux rope expands approximately self-similarly in the COR1 field of view of  $(1.5\text{--}4) R_\odot$ .

The true path of the prominence could be reconstructed from stereoscopic observations even when the angular separation between the STEREO spacecraft was as much as  $48^\circ$ . The reconstruction reveals that the dextral prominence rotated counter-clockwise by a large angle of  $\approx 115^\circ$  up to a heliocentric height of  $2.5 R_\odot$ , where the rotation leveled off. A gentle backward rotation by  $\approx 15^\circ$

---

may have followed in the height range up to  $3.3 R_{\odot}$ . Two thirds of the rotation were acquired within  $0.5 R_{\odot}$  from the photosphere. The coronal height profile of the rotation angle in a CME is thus derived for the first time. To our knowledge, this ranks as one of the largest rotations so far measured in the corona.

Taken jointly with recent results about the orientation of the CME at a heliocentric distance of  $\approx 13 R_{\odot}$ , obtained from fitting a croissant-shaped flux rope model to stereoscopic images from COR2 (Patsourakos and Vourlidas, 2011), a further counter-clockwise rotation by  $\approx 35^{\circ}$  from the value at  $2.5 R_{\odot}$  is indicated. This aligned the erupted flux closely with the heliospheric current sheet above the active region. However, the structure of the field within the first  $\sim 0.5 R_{\odot}$  above the original location of the prominence, obtained from a PFSS extrapolation, precludes alignment with the PIL as mechanism for the initial rotation.

The rotation and rise profiles of the prominence in the EUVI-COR1 height range are reproduced by a numerical model that follows the evolution of an unstable force-free flux rope. A parametric study of flux rope rotation in this model, detailed in Paper II, suggests that the main part of the rotation in this height range was caused by the shear field in the source volume. While the rotation and rise profiles can be modeled nearly equally well by a weakly kink-unstable flux rope of  $3.5\pi$  initial twist and by a kink-stable flux rope of  $2.5\pi$  initial twist, the indications of twist in the COR1 images and the absence of a strong initial perturbation in the EUVI-*Ahead* data favor the  $3.5\pi$  model, suggesting that the helical kink instability did occur and contributed the remaining part of the rotation.

In summary, the large total rotation of the erupting flux rope in the Cartwheel CME is due to a combination of three effects. The internal Lorentz forces associated with the shear field and with the tension of twisted field lines caused a strong rotation in the inner corona. The resulting orientation relative to the heliospheric current sheet was favorable for the subsequent alignment with the sheet in the outer corona and inner solar wind to proceed with the same sense of rotation. Since the heliospheric current sheet had an orientation relatively near the original direction of the erupting flux, a very large final rotation angle was reached.

**Acknowledgements** We acknowledge the use of data provided by the Global High Resolution H $\alpha$  Network, and by the SECCHI instruments on the STEREO spacecraft. Magnetic field extrapolations were supplied by the CCMC; special thanks to Lutz Rastaetter and Peter MacNeice for help with the CCMC data. We thank the anonymous referee for a constructive report which led to a deeper consideration of PIL orientation *vs.* height, and S. Patsourakos for information about his fitting of the CME orientation in the COR2 height range. WTT's work was supported by NASA Grant NNG06EB68C. BK's work was supported by the DFG, the STFC, and by NASA through Grant NNX08AG44G. TT's work was partially supported by the European Commission through the SOTERIA Network (EU FP7 Space Science Project No. 218816) and by the NASA HTP and LWS programs.

---

## References

Bi, Y., Jiang, Y.C., Yang, L.H., Zheng, R.S.: 2011, *New Astronomy* **16**, 276. doi:10.1016/j.newast.2010.11.009.

Culhane, J.L., Harra, L.K., James, A.M., Al-Janabi, K., Bradley, L.J., Chaudry, R.A., Rees, K., Tandy, J.A., Thomas, P., Whillock, M.C.R., Winter, B., Doschek, G.A., Korendyke, C.M., Brown, C.M., Myers, S., Mariska, J., Seely, J., Lang, J., Kent, B.J., Shaughnessy, B.M., Young, P.R., Simnett, G.M., Castelli, C.M., Mahmoud, S., Mapson-Menard, H., Probyn, B.J., Thomas, R.J., Davila, J., Dere, K., Windt, D., Shea, J., Haggard, R., Moye, R., Hara, H., Watanabe, T., Matsuzaki, K., Kosugi, T., Hansteen, V., Wikstol, Ø.: 2007, *Solar Phys.* **243**, 19. doi:10.1007/s01007-007-0293-1.

Dasso, S., Nakwacki, M.S., Démoulin, P., Mandrini, C.H.: 2007, *Solar Phys.* **244**, 115. doi:10.1007/s11207-007-9034-2.

Delaboudinière, J., Artzner, G.E., Brunaud, J., Gabriel, A.H., Hochedez, J.F., Millier, F., Song, X.Y., Au, B., Dere, K.P., Howard, R.A., Kreplin, R., Michels, D.J., Moses, J.D., Defise, J.M., Jamar, C., Rochus, P., Chauvineau, J.P., Marioge, J.P., Catura, R.C., Lemen, J.R., Shing, L., Stern, R.A., Gurman, J.B., Neupert, W.M., Maucherat, A., Clette, F., Cugnon, P., van Dessel, E.L.: 1995, *Solar Phys.* **162**, 291. doi:10.1007/BF00733432.

Golub, L., Deluca, E., Austin, G., Bookbinder, J., Caldwell, D., Cheimets, P., Cirtain, J., Cosmo, M., Reid, P., Sette, A., Weber, M., Sakao, T., Kano, R., Shibasaki, K., Hara, H., Tsuneta, S., Kumagai, K., Tamura, T., Shimojo, M., McCracken, J., Carpenter, J., Haight, H., Siler, R., Wright, E., Tucker, J., Rutledge, H., Barbera, M., Peres, G., Varisco, S.: 2007, *Solar Phys.* **243**, 63. doi:10.1007/s11207-007-0182-1.

Green, L.M., Kliem, B., Török, T., van Driel-Gesztelyi, L., Attrill, G.D.R.: 2007, *Solar Phys.* **246**, 365. doi:10.1007/s11207-007-9061-z.

Handy, B.N., Acton, L.W., Kankelborg, C.C., Wolfson, C.J., Akin, D.J., Bruner, M.E., Carvalho, R., Catura, R.C., Chevalier, R., Duncan, D.W., Edwards, C.G., Feinstein, C.N., Freeland, S.L., Friedlaender, F.M., Hoffmann, C.H., Hurlburt, N.E., Jurcevich, B.K., Katz, N.L., Kelly, G.A., Lemen, J.R., Levay, M., Lindgren, R.W., Mathur, D.P., Meyer, S.B., Morrison, S.J., Morrison, M.D., Nightingale, R.W., Pope, T.P., Rehse, R.A., Schrijver, C.J., Shine, R.A., Shing, L., Strong, K.T., Tarbell, T.D., Title, A.M., Torgerson, D.D., Golub, L., Bookbinder, J.A., Caldwell, D., Cheimets, P.N., Davis, W.N., Deluca, E.E., McMullen, R.A., Warren, H.P., Amato, D., Fisher, R., Maldonado, H., Parkinson, C.: 1999, *Solar Phys.* **187**, 229. doi:10.1023/A:1005166902804.

Harra, L.K., Crooker, N.U., Mandrini, C.H., van Driel-Gesztelyi, L., Dasso, S., Wang, J., Elliott, H., Attrill, G., Jackson, B.V., Bisi, M.M.: 2007, *Solar Phys.* **244**, 95. doi:10.1007/s11207-007-9002-x.

Howard, R.A., Moses, J.D., Vourlidas, A., Newmark, J.S., Socker, D.G., Plunkett, S.P., Korendyke, C.M., Cook, J.W., Hurley, A., Davila, J.M., Thompson, W.T., Cyr, O.C.S., Mentzell, E., Mehalick, K., Lemen, J.R., Wuelser, J.P., Duncan, D.W., Tarbell, T.D., Wolfson, C.J., Moore, A., Harrison, R.A., Waltham, N.R., Lang, J., Davis, C.J., Eyles, C.J., Mapson-Menard, H., Simnett, G.M., Halain, J.P., Defise, J.M., Mazey, E., Rochus, P., Mercier, R., Ravet, M.F., Delmotte, F., Auchere, F., Delaboudiniere, J.P., Bothmer, V., Deutsch, W., Wang, D., Rich, N., Cooper, S., Stephens, V., Maahs, G., Baugh, R., McMullin, D.: 2008, *Space Sci. Rev.* **136**, 67.

Isenberg, P.A., Forbes, T.G.: 2007, *Astrophys. J.* **670**, 1453.

Kliem, B., Török, T.: 2006, *Phys. Rev. Lett.* **96**, 255002.

Kliem, B., Török, T., Thompson, W.T.: 2011, *Solar Phys.*, to be submitted (Paper II).

Ko, Y., Raymond, J.C., Vrsnak, B., Vujic, E.: 2010, *Astrophys. J.* **722**, 625. doi:10.1088/0004-637X/722/1/625.

Landi, E., Raymond, J.C., Miralles, M.P., Hara, H.: 2010, *Astrophys. J.* **711**, 75. doi:10.1088/0004-637X/711/1/75.

Martin, S.F.: 1998, *Solar Phys.* **182**, 107. doi:10.1023/A:1005026814076.

Martin, S.F.: 2003, *Adv. Space Res.* **32**, 1883. doi:10.1016/S0273-1177(03)90622-3.

Martin, S.F., McAllister, A.H.: 1997, In: Crooker, N., Joselyn, J.A., Feynman, J. (eds.) *Coronal Mass Ejections: Causes and Consequences, Geophys. Monogr. Ser.* 99, AGU, Washington, D.C., 127.

Martin, S.F., Bilimoria, R., Tracadas, P.W.: 1994, In: R. J. Rutten & C. J. Schrijver (ed.) *Solar Surface Magnetism*, 303.

Muglach, K., Wang, Y., Kliem, B.: 2009, *Astrophys. J.* **703**, 976. doi:10.1088/0004-637X/703/1/976.

---

Patsourakos, S., Vourlidas, A.: 2011, *Astron. Astrophys.* **525**, A27+. doi:10.1051/0004-6361/201015048.

Pevtsov, A.A., Balasubramaniam, K.S., Rogers, J.W.: 2003, *Astrophys. J.* **595**, 500.

Plunkett, S.P., Vourlidas, A., Šimberová, S., Karlický, M., Kotrč, P., Heinzel, P., Kupryakov, Y.A., Guo, W.P., Wu, S.T.: 2000, *Solar Phys.* **194**, 371.

Priest, E.R., Forbes, T.G.: 2002, *Astron. Astrophys. Rev.* **10**, 313. doi:10.1007/s001590100013.

Rust, D.M., LaBonte, B.J.: 2005, *Astrophys. J.* **622**, 69.

Ruzmaikin, A., Martin, S., Hu, Q.: 2003, *J. Geophys. Res.* **108**, 1096. doi:10.1029/2002JA009588.

Savage, S.L., McKenzie, D.E., Reeves, K.K., Forbes, T.G., Longcope, D.W.: 2010, *Astrophys. J.* **722**, 329. doi:10.1088/0004-637X/722/1/329.

Török, T., Kliem, B., Titov, V.S.: 2004, *Astron. Astrophys.* **413**, 27.

Wang, Y., Muglach, K., Kliem, B.: 2009, *Astrophys. J.* **699**, 133. doi:10.1088/0004-637X/699/1/133.

Yurchyshyn, V.: 2008, *Astrophys. J.* **675**, 49. doi:10.1086/533413.

Yurchyshyn, V., Abramenko, V., Tripathi, D.: 2009, *Astrophys. J.* **705**, 426. doi:10.1088/0004-637X/705/1/426.